CHEMISTRY OF MATERIALS
Article
Cite This: Chem. Mater. 2017, 29, 9489-9497
pubs.acs.org/cm

Theory and Neutrons Combine To Reveal a Family of Layered Perovskites without Inversion Symmetry

Tong Zhu,[†] Toby Cohen,[†] Alexandra S. Gibbs,[‡] Weiguo Zhang,[§] P. Shiv Halasyamani,[§] Michael A. Hayward,*[,†] and Nicole A. Benedek*[,∥]

[†]Inorganic Chemistry Laboratory, Department of Chemistry, University of Oxford, South Parks Road, Oxford OX1 3QR, United Kingdom

[‡]ISIS Facility, Rutherford Appleton Laboratory, Chilton, Oxon OX11 0QX, United Kingdom

[§]Department of Chemistry, University of Houston, 112 Fleming Building, Houston, Texas 77204, United States

[∥]Department of Materials Science and Engineering, Cornell University, Ithaca, New York 14853, United States

Supporting Information

ABSTRACT: A flurry of recent theoretical studies have predicted the existence of new polar materials among several families of layered perovskites, including the double-layered Dion–Jacobson phases. These predictions have opened up exciting new opportunities for both fundamental studies of the crystal chemistry of Dion–Jacobson phases and their application as components in next-generation memories and low-power electronic devices. However, with some rare exceptions, all known double-layered Dion–Jacobson phases are nonpolar. We use an integrated theoretical–experimental approach to show that several Dion–Jacobson phases that have previously been synthesized and characterized as nonpolar are in fact polar. Additional theoretical calculations reveal that the polar phases of these materials emerge through a hybrid improper or trilinear coupling mechanism. Finally, our work has highlighted the critical role of neutron diffraction in characterizing the structures of double-layered Dion–Jacobson phases, which are typified by subtle oxygen atom displacements not easily resolved using even synchrotron X-ray diffraction.

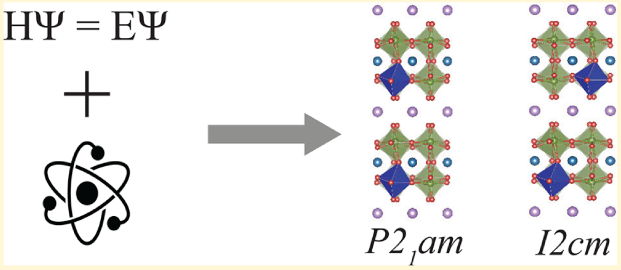

INTRODUCTION

From solar cells to high-capacity batteries, fuel cells, and next-generation memories, solid-state inorganic materials are at the heart of most energy and electronics technologies. However, the remarkable versatility of such materials can also present researchers with significant difficulties: for a given composition, there may exist several different structure types, typically only one of which (perhaps a metastable phase) has the desired properties for a given application. Indeed, the ability to design and direct atomic connectivity and crystal structure in the synthesis of target compounds is one of the most enduring challenges of inorganic materials chemistry. The development of soft chemistry and thin-film synthesis techniques has in some ways made the challenge only greater, because it is now possible to side step the thermodynamic limitations of traditional solid-state syntheses and produce metastable materials with new functionalities. Materials chemists are faced with a daunting multitude of targets: of all the possible compounds for a given stoichiometry and structure type, which ones have new or technologically relevant properties, and how can they be synthesized?

Layered perovskites are unparalleled among inorganic materials in the diversity of their structural, chemical, and physical properties. This family includes a number of excellent ionic conductors,[1,2] superconductors,[3] photoabsorbers[4] and electrocatalysts,[5] catalyst supports,[6] and noncentrosymmetric[7] and polar materials.[8−10] However, layered perovskites exist in various structure types and can accommodate a huge number of different compositions. In addition, the technologically relevant properties of layered perovskites often arise from subtle structural distortions, making structural characterization challenging. Guiding principles from theory, coupled with advanced synthesis and characterization techniques, are critical for identifying promising materials among the vast space of candidates.

In this work, we use an integrated theoretical–experimental approach to reveal the hidden potential of the Dion–Jacobson[11,12] (DJ) family of layered perovskites as multifunctional materials. The DJ phases form a homologous series with the general formula $A'[A_{n-1}B_nO_{3n+1}]$, where A′, A, and B are all different cations. As shown in Figure 1, A′ separates the n perovskite-like blocks and is typically a univalent ion, although metal halides,[13−16] metal chalcogenides,[17] alcohols,[18] polyethers,[19] carboxylates,[20] silicon-containing species,[21] and

Received: August 28, 2017
Revised: October 4, 2017
Published: October 4, 2017

DOI: 10.1021/acs.chemmater.7b03604
Chem. Mater. 2017, 29, 9489−9497

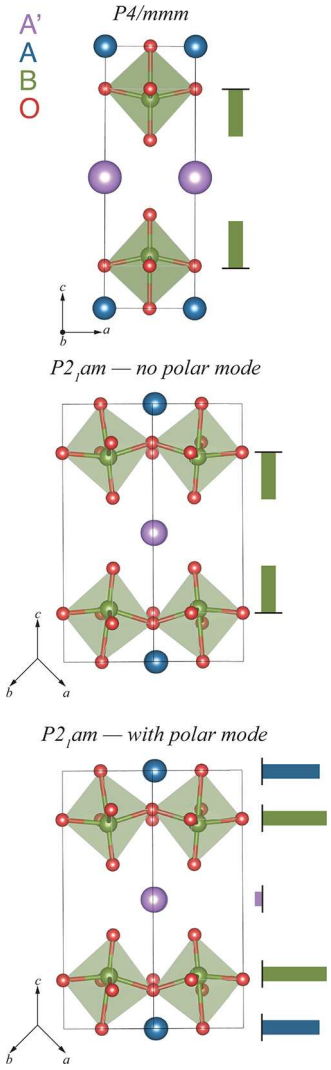

Figure 1. (Top) Structure of the high-symmetry *P*4/*mmm* aristotype for n = 2 Dion–Jacobson phases. The bars schematically indicate dipoles due to displacements of the Nb atoms along the c direction, which are equal in magnitude and oriented in opposite directions because of the inversion center in the A′ plane. The macroscopic polarization is thus zero. (Middle) Structure of the polar orthorhombic $P2_1am$ phase adopted by $CsBiNb_2O_7$, $RbBiNb_2O_7$, and $CsNdNb_2O_7$, with atomic displacements due to the polar Γ_5^- mode removed. Although the rotation modes by themselves break all inversion symmetries, the induced atomic displacements in the Nb–O layers are still equal and opposite. (Bottom) Polar $P2_1am$ phase with all allowed atomic displacements. There are now dipoles in all layers, aligned cooperatively along the orthorhombic a axis, thereby producing a nonzero macroscopic polarization. Note that the unit cell of the $P2_1am$ phase is larger than that of the aristotype; the lattice parameters of the polar phase are related to *P*4/*mmm* by a $\sqrt{2}a_T \times \sqrt{2}a_T \times c_T$ distortion, where a_T and c_T are the a and c lattice parameters of *P*4/*mmm*, respectively.

phosphorus-containing species[22] can also be intercalated into the interlayer space between perovskite blocks. DJ phases thus offer many more possibilities for chemical tuning by low-temperature cation exchange than, say, Ruddlesden–Popper (RP) phases, in which the di- and trivalent A cations are not so easily exchanged. However, in contrast to the RP and other families of layered perovskites, DJ phases have been comparatively little studied, perhaps because of the synthesis and characterization challenges that have obscured their promise as functional materials and led to many conflicting structural reports. Previous theoretical predictions[23,24] suggest that a number of double-layered n = 2 DJ phases that have been previously synthesized and characterized as nonpolar may in fact be polar, which has prompted a reexamination of past experimental work. In this work, we reexamine the structures and properties of $RbNdNb_2O_7$, $CsNdTa_2O_7$, and $RbNdTa_2O_7$ and demonstrate that all three phases are polar at room temperature by using synchrotron X-ray and neutron diffraction, in agreement with theoretical predictions. Interestingly, although the Rb-containing phases are found to be polar, they adopt structures that were not considered in previous work. Additional first-principles density functional theory (DFT) calculations confirm that the energies of the newly characterized structures are indeed lower than those proposed previously. Our calculations also show that, remarkably, although the space groups and relevant structural distortions of the Rb-containing phases differ in comparison to those of the Cs-containing phases, the mechanism driving the polar distortions is identical in both families of materials. Finally, our work highlights that high-resolution neutron diffraction is essential for accurately characterizing the structures of these DJ phases, which, along with many other families of layered perovskites, involve subtle displacements of the oxygen atoms. Critically, we found that even synchrotron X-ray diffraction experiments could not distinguish among several candidate space groups. We have shown that the DJ phases, possibly overlooked in the past because of incorrect structural refinements and a lack of guidance from theory, are promising targets for multifunctional materials, including ferroelectrics and multiferroics.

EXPERIMENTAL SECTION

DFT Calculations. First-principles calculations were performed using the Vienna Ab Initio Simulation Package (VASP).[25−28] The PBEsol exchange-correlation functional[29] and projector-augmented wave pseudopotentials[30,31] were used for all calculations. The valence electron configurations for each pseudopotential were as follows: $5s^25p^66s^1$ for Cs, $4s^24p^65s^1$ for Rb, $5s^25p^64f^16s^2$ for Nd (three f-electrons frozen in the core), $5s^25p^64d^45s^1$ for Nb, $5p^66s^25d^3$ for Ta, and $2s^22p^4$ for O. Structural relaxations were considered converged when the force on each atom became smaller than 1 meV/Å. A plane wave cutoff of 500 eV and a 6 × 6 × 4 Monkhorst–Pack mesh were used for all P-centered structures, whereas a 6 × 6 × 6 mesh was used for all I-centered structures. Force constants were calculated using the finite displacement method (and checked using density functional perturbation theory), as described in ref 24. The total macroscopic polarization $\mathcal{P}$ for each material in the relevant polar space group was calculated using the expression[32]

$$\mathcal{P} = \frac{|e|}{\Omega}\sum_s Z_s^* \mathbf{u}_s \quad (1)$$

where $|e|$ is the electron charge, Ω is the unit cell volume, Z_s^* is the Born effective charge tensor of atom s in the *P*4/*mmm* reference structure (calculated using density functional perturbation theory), and $\mathbf{u}_s$ is the displacement of atom s from its position in the *P*4/*mmm* aristotype structure. This is a linear approximation to the polarization, the fidelity of which has been explicitly verified for perovskites.[32] Crystallographic analyses were performed with the aid of the ISOTROPY suite of programs,[33] and the Bilbao Crystallographic Server.[34,35]

Synthesis. Powder samples of $RbNdNb_2O_7$, $CsNdTa_2O_7$, and $RbNdTa_2O_7$ were prepared via a ceramic synthesis method from Rb_2CO_3 (99.8%), Cs_2CO_3 (99.994%), Nd_2O_3 (99.99%), Nb_2O_5

DOI: 10.1021/acs.chemmater.7b03604
Chem. Mater. 2017, 29, 9489−9497

(99.9985%), and Ta_2O_5 (99.993%). Nd_2O_3, Nb_2O_5, and Ta_2O_5 were dried at 900 °C before being used. A suitable stoichiometric ratio of the oxides was ground together in an agate pestle and mortar and then combined with a 50% excess of Rb_2CO_3 or Cs_2CO_3 (to compensate for metal loss due to the volatility of these reagents). These mixtures were then heated at 850 °C in air for 12 h, reground, and pressed into pellets. Samples of $RbNdNb_2O_7$ were heated in air for four periods of 48 h at 1000 °C and a further 48 h at 1050 °C. Samples of $RbNdTa_2O_7$ and $CsNdTa_2O_7$ were heated in air for four periods of 48 h at 1050 °C. All samples were reground and pressed into pellets between heating cycles. As a final step, all samples were washed in distilled water, to remove any remaining excess Rb or Cs oxides, and then dried for 12 h at 140 °C in air.

Characterization. Reaction progress and final sample purity were assessed by X-ray powder diffraction data collected using a PANalytical X'pert diffractometer incorporating an X'celerator position sensitive detector (monochromatic Cu $K\alpha_1$ radiation). High-resolution synchrotron X-ray powder diffraction patterns were collected using instrument I11 at Diamond Light Source Ltd. Diffraction patterns were measured using Si-calibrated X-rays with an approximate wavelength of 0.825 Å, from samples sealed in 0.3 mm diameter borosilicate glass capillaries. Neutron powder diffraction data were collected from samples contained within vanadium cans, using the HRPD diffractometer (ISIS neutron source). Rietveld profile refinement was performed using the GSAS suite of programs.[36] The particle size-dependent second-harmonic generation (SHG) response of samples was measured by grinding sintered pellets of material and then sieving the resulting powders into distinct particle size ranges (<20, 20−45, 45−63, 63−75, 75−90, and 90−25 μm). The SHG intensity was then recorded from each particle size range and compared to that of a standard sample of KH_2PO_4 (KDP) in the same particle size ranges. No index matching fluid was used in any of the experiments. A detailed description of the experimental setup and process has been reported previously.[37]

RESULTS AND DISCUSSION

Origin of Polar Structures in the Dion−Jacobson Family. New insights gained from recent experimental and theoretical studies have led to the formulation of design principles for polar and noncentrosymmetric layered perovskites. In particular, previous work that focused on polar materials has highlighted the key role played by nonpolar structural distortions, commonly rotations or twists of the transition metal octahedra, in driving the emergence of polar phases in the RP,[9,38−40] DJ,[23,41−43] Aurivillius,[44−48] and double-perovskite[49−54] families. Among the n = 2 DJ phases, only $CsBiNb_2O_7$,[41] $RbBiNb_2O_7$,[55] and $CsNdNb_2O_7$[41] have been observed to form in polar space groups; polarization-field hysteresis has been demonstrated[55] for $RbBiNb_2O_7$, and some evidence of ferroelectricity has been presented for $CsBiNb_2O_7$.[56] $CsLaNb_2O_7$, $CsLaTa_2O_7$, $RbLaNb_2O_7$, and $RbLaTa_2O_7$ have been shown experimentally to be at least noncentrosymmetric[57] (though perhaps nonpolar), though their crystal structures have not been definitively determined. All of these materials, except for $CsNdNb_2O_7$ and the two Bi-containing compounds, were initially reported to adopt the undistorted $P4/mmm$ aristotype structure.

Recent theoretical predictions suggest that there may be more polar materials among the DJ phases than previously appreciated.[24,58] Benedek[24] used first-principles density functional theory calculations, in combination with symmetry principles, to show that the energy of the polar $P2_1am$ space group adopted by $CsNdNb_2O_7$ and the Bi-containing compounds is signficantly lower than that of the $P4/mmm$ structure for the series $A'ANb_2O_7$ (A′ = Cs or Rb, and A = La, Nd, or Y). We report in this work that the polar $P2_1am$ phase is also a low-energy structure for $CsNdTa_2O_7$ and $RbNdTa_2O_7$; both materials were assigned to the $P4/mmm$ space group in prior work.[59−61] Table 1 summarizes our theoretical results in the context of previous experimental findings.

Table 1. Energy Difference (per formula unit) from Our DFT Calculations between Fully Relaxed $P4/mmm$ Artistotype and Distorted Polar $P2_1am$ Structures with a Summary of Previous Experimental Findings[a]

compound	ΔE (meV/formula unit)	comments
$CsNdTa_2O_7$	−267	nonpolar ($P4/mmm$) from previous experiments[59−61]
$RbNdTa_2O_7$	−297	nonpolar ($P4/mmm$) from previous experiments[59−61]
$CsNdNb_2O_7$	−320	polar ($P2_1am$) from previous experiments[41]
$RbNdNb_2O_7$	−349	nonpolar ($P4/mmm$) from previous experiments[62,63]

[a]Negative energy differences indicate that the polar $P2_1am$ phase is more stable than the $P4/mmm$ phase. Theoretical data for $CsNdNb_2O_7$ and $RbNdNb_2O_7$ were first reported in ref 24.

The hybrid improper mechanism has been shown to account for the preference of these materials to adopt a distorted polar structure over the undistorted aristotype.[24] Briefly, the transition to a polar structure in materials that exhibit this mechanism is driven by combinations of symmetry-distinct nonpolar lattice distortions, which couple to a polar mode. In the discussion that follows, we use both Glazer notation[64] and group theoretical mode labels[65−67] to denote different structural distortions. In the case of the DJ phases, the symmetry of the $P2_1am$ phase is established by two different rotations, one mode transforming like the irreducible representation (irrep) M_2^+ ($a^0a^0c^+$-like rotation) and one mode transforming like M_5^- ($a^-a^-c^0$-like rotation). These two nonpolar modes by themselves break all inversion symmetries to produce polar space group $P2_1am$; however, as the middle panel of Figure 1 shows, the macroscopic polarization due to ionic displacements is still zero (these modes do produce local dipoles in the Nb−O layers, but they are oriented in equal and opposite directions and thus cancel each other out). It is the coupling of the two rotation modes to the polar Γ_5^- mode that produces a macroscopic polarization (bottom panel of Figure 1). Although the phenomenological aspects of hybrid improper ferroelectricity have been described in several previous publications,[48,54,68−70] its crystal chemical basis can be difficult to visualize. An especially important aspect of this mechanism is that the origin of the transition from the nonpolar to polar phase is not chemical hybridization, in contrast with classical perovskite ferroelectrics such as $BaTiO_3$, where the transition to the polar phase is driven by charge transfer between the formally empty Ti 3d states and the filled O 2p states.[71] Instead, nonpolar rotation modes are the primary drivers of the transition to the polar phase in the majority of hybrid improper materials that have been studied so far. These distortions generally arise from electrostatic or ion size-mismatch effects and optimize the A cation coordination environment, which is underbonded in the high-symmetry aristotype structure. Hence, hybrid improper ferroelectrics need not contain a ferroelectrically active d^0 or lone pair cation. The reader should keep this in mind throughout the discussion that follows because all the materials studied here do in fact contain ferroelectrically active

DOI: 10.1021/acs.chemmater.7b03604
Chem. Mater. 2017, 29, 9489−9497

cations (Nb^{5+} $4d^0$ and Ta^{5+} $5d^0$). However, as Figure 1 illustrates, although d−p hybridization contributes to the total polarization for these materials (by inducing displacements of the Nb and Ta atoms), it is not the driving force.

Structural Characterization. To test the theoretical predictions discussed above, $CsNdTa_2O_7$, $RbNdNb_2O_7$, and $RbNdTa_2O_7$ were synthesized and synchrotron X-ray powder diffraction data collected. All three materials could be indexed using orthorhombic unit cells, which are an approximate $\sqrt{2} \times \sqrt{2} \times 1$ geometric expansion on the aristotype Dion−Jacobson unit cell. Close inspection revealed very weak additional diffraction peaks in the diffraction data collected from the two rubidium-containing samples, suggesting a further doubling of the *c* axis to give a $\sqrt{2} \times \sqrt{2} \times 2$ expanded cell consistent with the *Imam* symmetry, $a^-a^-c^0/-a^--a^-c^0$ distorted structure reported for $RbLaNb_2O_7$[72] (the rotation pattern after the forward slash refers to that in neighboring perovskite blocks; in this case, the rotation pattern is the same in neighboring blocks but of the opposite phase or sense, which is denoted by the prefactor minus signs). However, comparing Rietveld refinements using models based on the $P2_1am$, $a^-a^-c^+$ distorted structure of $CsNdNb_2O_7$[41] and the *Imam* distorted structure of $RbLaNb_2O_7$ revealed that both models gave fits of statistically equivalent quality to the data collected from all three samples, as described in detail in the Supporting Information. These results demonstrate that even high-resolution synchrotron X-ray powder diffraction data are not capable of accurately determining the distorted structures of Dion−Jacobson phases. We have therefore used a combination of SHG measurements and neutron diffraction data to structurally characterize these phases.

Measurements show that $RbNdNb_2O_7$, $CsNdTa_2O_7$, and $RbNdTa_2O_7$ all exhibit SHG activity (see Figure 2 for data for $RbNdNb_2O_7$), which increases with an increase in particle size (Figures S6 and S7), indicating that all three phases adopt noncentrosymmetric crystal structures. High-resolution neutron powder diffraction data collected from $CsNdTa_2O_7$ can be unambiguously indexed using a primitive, orthorhombic unit cell that is a $\sqrt{2} \times \sqrt{2} \times 1$ geometric expansion of the aristotype cell, with extinction conditions consistent with noncentrosymmetric space group $P2_1am$, as shown in the bottom panel of Figure 1. A model based on the reported structure of $CsNdNb_2O_7$ was refined against these data to give a good statistical fit, confirming that $CsNdNb_2O_7$ and $CsNdTa_2O_7$ are isostructural.[41]

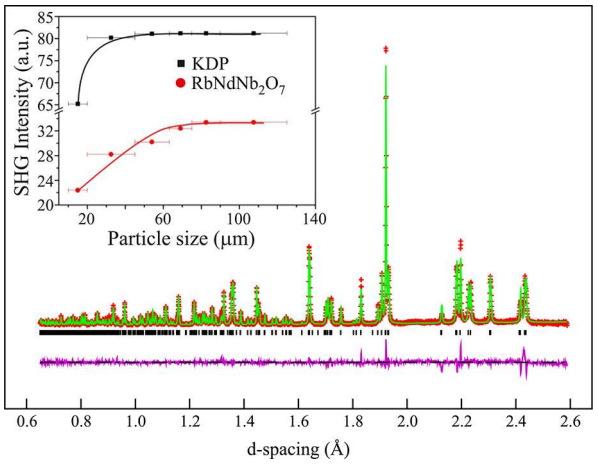

Figure 2. Observed, calculated, and difference plots from the structural refinement of $RbNdNb_2O_7$ using an *I2cm* model, against neutron powder diffraction data (χ^2 = 8.23). The inset shows a plot of SHG activity of $RbNdNb_2O_7$ as a function of particle size, compared to that of a KH_2PO_4 (KDP) standard.

In contrast, neutron powder diffraction data collected from $RbNdNb_2O_7$ and $RbNdTa_2O_7$ could both be indexed using only an orthorhombic cell with a $\sqrt{2} \times \sqrt{2} \times 2$ expansion of the aristotype cell, and extinction conditions consistent with a body-centered space group. While the observed cell expansion and symmetry are compatible with an $a^-a^-c^0/-(a^-a^-c^0)$ distorted structure, the observation of SHG activity in both phases is incompatible with this centrosymmetric distortion. However, the addition of an in-phase rotation of the MO_6 octahedra around the *z* axis to give an $a^-a^-c^+/-(a^-a^-c^+)$ distortion fits the crystallographic criteria and results in polar space group *I2cm*. Thus, structural models based on this distortion type were refined against the neutron diffraction data collected from $RbNdNb_2O_7$ and $RbNdTa_2O_7$ and gave good statistical fits in both cases. Full details of the refined structures of $CsNdTa_2O_7$, $RbNdNb_2O_7$, and $RbNdTa_2O_7$ are given in Tables S1−S3, along with parameters from the structural refinements (Tables S4−S6), selected bond lengths (Tables S7−S9), and plots of the observed and calculated data (Figures S1−S5 and S8−S10).

Theory Revisited. A polar *I2cm* structure has not been considered in prior theoretical works, nor have any previously synthesized *n* = 2 Dion−Jacobson phases been reported in this space group, as far as we are aware. Why do the Rb-containing compounds adopt structures that differ from those of their Cs-containing counterparts? To answer this question, we first checked whether the energy of the *I2cm* phase is indeed lower than that of the $P2_1am$ phase. Table 2 shows that in the case of $CsNdTa_2O_7$ and $CsNdNb_2O_7$, the energy of the $P2_1am$ phase is lower than that of the *I2cm* phase, whereas the opposite is true for $RbNdTa_2O_7$ and $RbNdNb_2O_7$. Table 2 also shows the polarization from our first-principles calculations for the lowest-energy polar phase of each material. We note that polarization switching in layered perovskites is more complex than in structurally simpler ferroelectrics (such as $PbTiO_3$, for example), and hence, experimentally measured polarization values will likely deviate from those listed in Table 2. We therefore provide the polarization values as estimates and to demonstrate trends as a function of composition.

Table 2. Energy Differences (in millielectronvolts per formula unit) between the Aristotype *P4/mmm* and Selected Distorted Phases and Total Macroscopic Polarizations for the Lowest-Energy Polar Phase for Nb- and Ta-Containing Compositions

	ΔE (meV/formula unit)		
	$P2_1am$	*I2cm*	$\mathcal{P}$ (μC cm^{-2})
$RbNdNb_2O_7$	−349	−360	30
$RbNdTa_2O_7$	−297	−307	25
$CsNdNb_2O_7$	−320	−309	29
$CsNdTa_2O_7$	−267	−258	23

It seemed reasonable to assume that there must be some structural reason for the differences between the two sets of compounds, so we calculated bond valence sums for the cations and for the apical oxygens that point into the interlayer gallery for $RbNdNb_2O_7$ and $CsNdNb_2O_7$ in both the $P2_1am$ and *I2cm*

DOI: 10.1021/acs.chemmater.7b03604
Chem. Mater. 2017, 29, 9489−9497

space groups. However, as Table 3 shows, although there are some differences in the bond valence sums between the two structure types, they are generally too small to be significant.

Table 3. Bond Valence Sums (in valence units) for the Polar $P2_1am$ and $I2cm$ Phases for $RbNdNb_2O_7$ and $CsNdNb_2O_7$[a]

	$P2_1am$	$I2cm$
	$RbNdNb_2O_7$	
Rb	0.91	0.93
Nd	3.09	3.09
Nb	4.93	4.92
O	−1.90	−1.91
	$CsNdNb_2O_7$	
Cs	1.13	1.14
Nd	3.06	3.05
Nb	4.91	4.91
O	−2.01	−2.01

[a]The bond valence sum for oxygen refers to the apical oxygen atom that points into the interlayer gallery between perovskite blocks.

The $P2_1am$ structure adopted by $CsNdNb_2O_7$ is characterized by an $a^-a^-c^+$ rotation pattern in each perovskite double layer, with the origin of adjacent layers related by a simple primitive $(0,0,{}^1/_2)$ stacking. In contrast, $RbNdNb_2O_7$ adopts an $I2cm$ structure with the same $a^-a^-c^+$ cooperatively distorted perovskite double layers, but these are now stacked with a $({}^1/_2,0,{}^1/_2)$ origin shift to give an overall distortion of $a^-a^-c^+/-(a^-a^-c^+)$. We can see why the Rb phase adopts the $({}^1/_2,0,{}^1/_2)$ stacking of layers by comparing the (experimentally) refined structure to a hypothetical structure in which the perovskite double layers in the refined $I2cm$ structure are now stacked in a primitive way, as shown in Figure 3. Note that this is not exactly the same as the $P2_1am$ structure because there are more degrees of freedom to displace the Rb and Nd centers in $P2_1am$.

As the perovskite double layers are identical in the refined and hypothetical structures, it follows that both the Nb−O and Nd−O bond lengths are identical in both structures, and the only difference lies in the Rb−O layers. Considering the Rb−O bond lengths (Figure 4), we can see the symmetry relationship between the two stacking types leads to equivalent Rb−O bond lengths, and thus identical bond valence sums for Rb, in the refined and hypothetical structures. However, the $({}^1/_2,0,{}^1/_2)$ displacement in the $I2cm$ stacking means that the "opposed" oxide ions (the apical oxygen atoms that point into the interlayer gallery) are displaced in opposite directions, compared to the primitive stacking where they are displaced in the same direction. As a result, the O−O distances in the $I2cm$ structure are larger than in the primitively stacked structure, even though the Rb bond valence sums are the same for both structures. Hence, via adoption of the $I2cm$-type stacking, the O−O bond lengths can be increased without changing the Rb−O bond lengths, an obvious advantage.

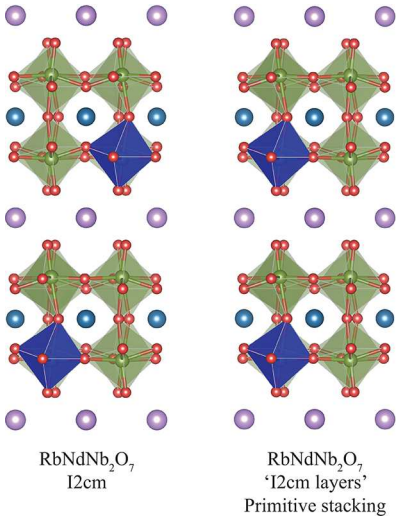

Figure 3. Refined (left) and hypothetical (right) structures of $RbNdNb_2O_7$. Equivalent Nb−O polyhedra are colored blue in both structures to illustrate the differences in stacking between adjacent perovskite blocks in the two different structures. The coloring scheme is otherwise identical to that in Figure 1.

Given the advantage in adopting the $I2cm$ structure, the question then becomes why does $CsNdNb_2O_7$ not do this? Again, we can make a comparison between the refined $P2_1am$ structure of $CsNdNb_2O_7$ and a hypothetical structure in which the same perovskite double layers are stacked with a $({}^1/_2,0,{}^1/_2)$ displacement to yield a stacking pattern analogous to that of the $I2cm$ structure. We note again that the additional degrees of freedom in the $P2_1am$ layers mean that this hypothetical structure is not exactly the same as the $I2cm$ structure. The only difference between these refined and hypothetical structures also lies in the Cs−O layer. However, now when we look at the CsO_8 polyhedra (Figure 5) in the two structures, the additional displacement of the Cs centers in $P2_1am$ (the Wyckoff site for the alkali cation has two free parameters in $P2_1am$ and only one in $I2cm$) leads to different Cs−O bond lengths in the two stacking configurations. The additional displacement of the Cs in the $P2_1am$ structure means that when the perovskite double layers are stacked with a $({}^1/_2,0,{}^1/_2)$ displacement, a very short Cs−O bond length is formed, and the CsO_8 site is too small for Cs in this configuration.

The choice between adopting the $P2_1am$ or $I2cm$ structures is thus a compromise. The rare earth cation size dictates which cooperative rotation pattern is adopted by the Nb−O framework (the Nb−O frameworks of $CsNdNb_2O_7$ and $RbNdNb_2O_7$ are remarkably similar), but the stacking of adjacent layers, primitive versus $({}^1/_2,0,{}^1/_2)$, is determined by the identity of the A′ cation. The $I2cm$ structure minimizes O−O repulsion between the apical oxide ions but forces the A′ cation into a high-symmetry site, potentially compromising the bonding in the $A'O_8$ polyhedron. The $P2_1am$ structure allows the A′ cation more degrees of freedom to displace within the $A'O_8$ polyhedron but has greater apical O−O repulsion.

In summary, $RbNdNb_2O_7$ adopts the $I2cm$ structure because it can satisfy the local bonding requirements of both Nd and Rb without the need for additional A and A′ cation displacements and therefore opts for a $({}^1/_2,0,{}^1/_2)$ stacking to minimize O−O repulsion. In contrast, the larger difference in size between the A and A′ cations in $CsNdNb_2O_7$ means that it is beneficial to utilize the extra degree of freedom in the A and A′ displacements to optimize their local coordinations even though this leads to enhanced O−O repulsion. Even when this is done, the cation coordinations are still quite strained (Nd BVS = 3.16, Cs = 1.07 in the experimentally refined structure). In other words, rotations by themselves cannot simultaneously optimize the A and A′ coordination environments for the Cs-containing phases, so additional degrees of freedom (cation displacements) are required to relieve bond strain at these sites.

DOI: 10.1021/acs.chemmater.7b03604
Chem. Mater. 2017, 29, 9489−9497

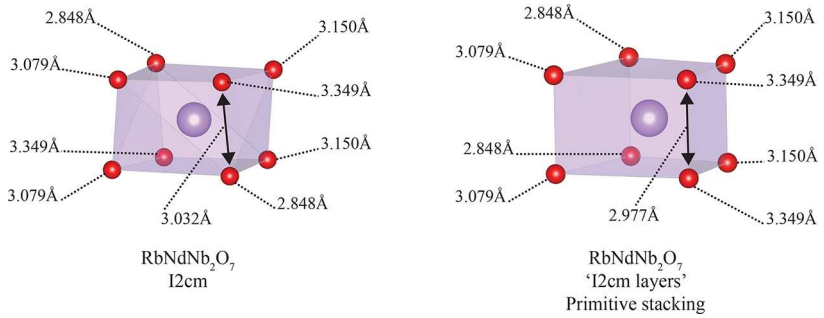

Figure 4. Rb−O coordination polyhedra of the refined (left) and hypothetical (right) structures of $RbNdNb_2O_7$ shown in Figure 3. Each RbO_8 polyhedron has the same eight Rb−O bond lengths, but the arrangement in the refined *I2cm* model results in longer O−O separations, denoted by the double-headed arrows.

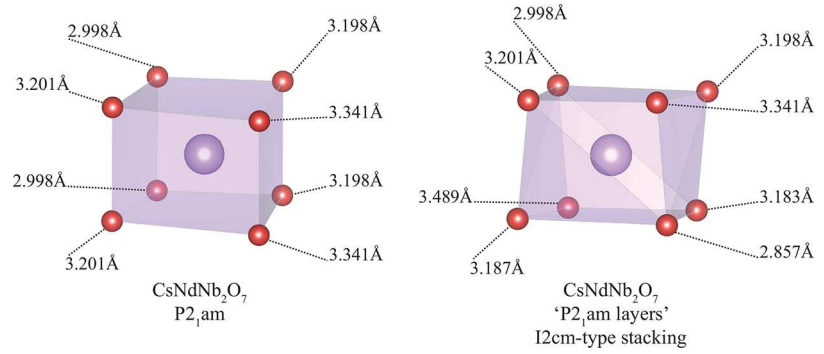

Figure 5. Cs−O coordination polyhedron of the refined (left) and hypothetical (right) structures of $CsNdNb_2O_7$.

If our reasoning presented above is correct, then the $P2_1am$ structure should become increasingly favorable as the difference in size between the A (rare earth) and A′ cations increases. An additional set of first-principles calculations shows that this is indeed the case. Table 4 shows that for the Cs-containing compounds, the difference in energy between the $P2_1am$ and *I2cm* structures increases as the size of the A cation decreases. By the time A = Y, there is a very large size difference between the A and A′ cations and the structure needs all available degrees of freedom (cation displacements) to relieve bond strain at as many sites as possible. It is willing to "pay the price" in terms of O−O repulsion to achieve this. In contrast, the Rb-containing compounds show the opposite trend. As the A cation size decreases, the difference in energy between the $P2_1am$ and *I2cm* space groups decreases. This is because rotations are initially enough to satisfy the bonding preferences of both the A and A′ sites, so the Rb systems adopt the *I2cm* structure because it results in less O−O repulsion, as discussed above. However, as the size of the A cation decreases, the Rb-containing phases run into the same problem as the Cs-containing materials. Rotations can no longer efficiently relieve bond strain at both the A and A′ sites, so the *I2cm* structure is not as favorable as it is for larger A cation sizes. Given the synthetic and chemical constraints of real materials, i.e., when the difference in size between the A and A′ cations becomes very large, a structure (or mixture of structures) other than a DJ phase will probably be formed; Cs-containing phases will likely always adopt the $P2_1am$ structure, whereas Rb-containing phases will likely always adopt the *I2cm* structure.

Table 4. Differences in Energy between the Aristotype *P4/mmm* Phase and Distorted Phases for a Series of Cs- and Rb-Containing Materials from First-Principles Calculations[a]

	$P2_1am$ (meV/formula unit)	*I2cm* (meV/formula unit)
$CsLaNb_2O_7$	−102	−96
$CsNdNb_2O_7$	−320	−309
$CsYNb_2O_7$	−1017	−998
$RbLaNb_2O_7$	−119	−131
$RbNdNb_2O_7$	−349	−360
$RbYNb_2O_7$	−1064	−1072

[a]Negative energy differences indicate that the distorted phase is more stable than the aristotype.

Mechanism. Now that we have established the crystal chemical origin of the preference of the Rb-containing materials for the *I2cm* structure, we consider the mechanism through which the polar phase emerges. Is it through a hybrid improper mechanism, or via some other route? A symmetry analysis can provide some immediate clues. The polar *I2cm* phase is related to the parent *P4/mmm* aristotype by a combination of distortion modes transforming like irreps A_2^+ and A_5^-. These modes arise at the *A*-point of the primitive tetragonal Brillouin zone with wave vector $\mathbf{k} = (^1/_2,^1/_2,^1/_2)$, which means that distortions associated with the *A*-point will double the *P4/mmm* unit cell along all three crystallographic axes. The A_5^- mode is analogous to the M_5^- distortion and corresponds to an $a^-a^-c^0/-(a^-a^-c^0)$ rotation pattern. Similarly, the A_2^+ mode is analogous to the M_2^+ distortion and corresponds to an $a^0a^0c^+/-(a^0a^0c^+)$ rotation pattern. Crucially, the combination of the A_5^- and A_2^+ modes establishes the symmetry of the *I2cm* space group, and these modes also couple to the polar Γ_5^- mode. This is precisely the situation for DJ phases that adopt the $P2_1am$ space group and suggests that the *I2cm* structure of the Rb-containing materials also emerges through a trilinear coupling or hybrid improper mechanism. However, the fact that the A_2^+

DOI: 10.1021/acs.chemmater.7b03604
Chem. Mater. 2017, 29, 9489−9497

Table 5. Force Constants of Listed Modes for Rb-Containing Materials in the *P*4/*mmm* Space Groups and Differences in Energy between Fully Relaxed and Distorted Structures[a]

	force constant (eV/Å^2)			ΔE (meV/formula unit)			
material	A_5^-	A_2^+	Γ_5^-	*Imma*	*I*4/*mcm*	*C*2*mm*	*I*2*cm*
$RbNdNb_2O_7$	−2.347	−0.486	−0.866	−206	−69	−7	−360
$RbNdTa_2O_7$	−2.206	−0.416	−0.610	−179	−47	−3	−307

[a]*Imma* is the space group that results from freezing in the A_5^- mode along the direction required to produce the *I*2*cm* space group when combined with the A_2^+ and Γ_5^- modes (*I*4/*mcm* results from freezing in the A_2^+ mode, and polar group *C*2*mm* results from freezing in the Γ_5^- mode). Results for the force constant and energy lowering of the Γ_5^- mode for $RbNdNb_2O_7$ were originally reported in ref 24.

and A_5^- modes are allowed by symmetry does not mean that they are energetically favorable.

We determined the tendency of the Rb-containing compounds to undergo A_2^+ and A_5^- distortions by calculating the force constants of these modes. Table 5 shows that both $RbNdNb_2O_7$ and $RbNdTa_2O_7$ are unstable to A_2^+, A_5^-, and Γ_5^- distortions in the *P*4/*mmm* structure; that is, freezing these modes into the aristotype *P*4/*mmm* structure lowers the energy of the crystal in each case. However, Table 5 also shows that although each mode individually lowers the energy, the largest increase in energy comes from combining the A_2^+, A_5^-, and Γ_5^- modes to form the *I*2*cm* structure. This strongly suggests that the *I*2*cm* phase of these Rb-containing materials emerges through the same trilinear coupling mechanism that produces the $P2_1am$ structure of the Cs-containing materials. With so many different modes involved, the phase transition and critical behavior may become somewhat complex; this will be reported in a forthcoming publication.

CONCLUSIONS

We have used a combination of first-principles calculations, synthesis, and characterization experiments to show that the Dion−Jacobson family may potentially host a number of polar and multifunctional materials. Our work has revealed that $CsNdTa_2O_7$, $RbNdTa_2O_7$, and $RbNdNb_2O_7$, all initially characterized as adopting nonpolar structures, do in fact form in polar space groups, although the Cs-containing phases prefer a structure different from that of the Rb-containing phases. The crystal chemical origins of this difference are rather subtle but essentially involve a competition between the bonding preferences of the A and A′ cations. When the difference between the sizes of these two cations is large, as in the Cs-containing materials, then octahedral rotations alone cannot satisfy their bonding requirements and additional cation displacements, allowed in $P2_1am$, help to relieve bond strain. In contrast, the smaller size difference between the A and A′ cations in the Rb-containing compounds means that octahedral rotations can simultaneously optimize both coordination environments, so the *I*2*cm* structure, which minimizes apical O−O repulsion, is preferred. We have also shown that although the Cs- and Rb-containing materials adopt different polar structures, the mechanism through which these phases emerge appears to be identical, namely, the hybrid improper or trilinear coupling mechanism. The literature already contains a significant number of reports of $n = 2$ Dion−Jacobson phases; we suggest that these materials be revisited, by both theorists and experimentalists, as there are likely additional polar phases to be discovered. The possibilities offered by topochemical techniques (synthesizing a polar phase with magnetic ions, for example) only expand the opportunities for materials design and discovery in the Dion−Jacobson family.

ASSOCIATED CONTENT

Supporting Information

The Supporting Information is available free of charge on the ACS Publications website at DOI: 10.1021/acs.chemmater.7b03604.

Plots of SHG activity as a function of particle size for $CsNdTa_2O_7$ and $RbNdTa_2O_7$; structural refinement data for $RbNdNb_2O_7$, $CsNdTa_2O_7$, and $RbNdTa_2O_7$; parameters from the structural refinements of $RbNdNb_2O_7$, $CsNdTa_2O_7$, and $RbNdTa_2O_7$ against neutron diffraction data collected at 298 K; and selected bond lengths from the refined structures of $RbNdNb_2O_7$, $CsNdTa_2O_7$, and $RbNdTa_2O_7$ (PDF)

AUTHOR INFORMATION

Corresponding Authors

*E-mail: michael.hayward@chem.ox.ac.uk.
*E-mail: nbenedek@cornell.edu. Phone: +1 607-255-6429. Fax: +1 607-255-2365.

ORCID

P. Shiv Halasyamani: 0000-0003-1787-1040
Michael A. Hayward: 0000-0002-6248-2063
Nicole A. Benedek: 0000-0001-5026-5574

Notes

The authors declare no competing financial interest.

ACKNOWLEDGMENTS

N.A.B. was supported by the National Science Foundation (NSF) via Grant DMR-1550347. This work used the Extreme Science and Engineering Discovery Environment (XSEDE), which is supported by NSF Grant ACI-1548562, and the high-performance computing facilities of the Cornell Center for Advanced Computing. Experiments at the ISIS pulsed neutron facility were supported by a beam time allocation from the Science and Technology Facilities Council. Experiments at the Diamond Light Source were performed as part of the Block Allocation Group award "Oxford Solid State Chemistry BAG to probe composition-structure-property relationships in solids" (EE13284). W.Z. and P.S.H. thank the Welch Foundation (Grant E-1457) and the National Science Foundation (DMR-1503573).

REFERENCES

(1) Schaak, R. E.; Mallouk, T. E. Topochemical Synthesis of Three-Dimensional Perovskites from Lamellar Precursors. *J. Am. Chem. Soc.* **2000**, *122*, 2798−2803.

(2) Yashima, M.; Enoki, M.; Wakita, T.; Ali, R.; Matsushita, Y.; Izumi, F.; Ishihara, T. Structural Disorder and Diffusional Pathway of Oxide Ions in A Doped Pr_2NiO_4-Based Mixed Conductor. *J. Am. Chem. Soc.* **2008**, *130*, 2762−2763.

DOI: 10.1021/acs.chemmater.7b03604
Chem. Mater. 2017, 29, 9489−9497

(3) Müller-Buschbaum, H. The Crystal Chemistry of High-Temperature Oxide Superconductors and Materials with Related Structures. *Angew. Chem., Int. Ed. Engl.* **1989**, *28*, 1472−1493.
(4) Stoumpos, C. C.; Cao, D. H.; Clark, D. J.; Young, J.; Rondinelli, J. M.; Jang, J. I.; Hupp, J. T.; Kanatzidis, M. G. Ruddlesden-Popper Hybrid Lead Iodide Perovskite 2D Homologous Semiconductors. *Chem. Mater.* **2016**, *28*, 2852−2867.
(5) Takeguchi, T.; Yamanaka, T.; Takahashi, H.; Watanabe, H.; Kuroki, T.; Nakanishi, H.; Orikasa, Y.; Uchimoto, Y.; Takano, H.; Ohguri, N.; Matsuda, M.; Murota, T.; Uosaki, K.; Ueda, W. Layered Perovskite Oxide: A Reversible Air Electrode for Oxygen Evolution/Reduction in Rechargeable Metal-Air Batteries. *J. Am. Chem. Soc.* **2013**, *135*, 11125−11130.
(6) Strayer, M. E.; Binz, J. M.; Tanase, M.; Kamali Shahri, S. M.; Sharma, R.; Rioux, R. M.; Mallouk, T. E. Interfacial Bonding Stabilizes Rhodium and Rhodium Oxide Nanoparticles on Layered Nb and Ta Oxide Supports. *J. Am. Chem. Soc.* **2014**, *136*, 5687−5696.
(7) Akamatsu, H.; Fujita, K.; Kuge, T.; Sen Gupta, A.; Togo, A.; Lei, S.; Xue, F.; Stone, G.; Rondinelli, J. M.; Chen, L.-Q.; Tanaka, I.; Gopalan, V.; Tanaka, K. Inversion Symmetry Breaking by Oxygen Octahedral Rotations in the Ruddlesden-Popper $NaRTiO_4$ Family. *Phys. Rev. Lett.* **2014**, *112*, 187602.
(8) Pitcher, M. J.; Mandal, P.; Dyer, M. S.; Alaria, J.; Borisov, P.; Niu, H.; Claridge, J. B.; Rosseinsky, M. J. Tilt Engineering of Spontaneous Polarization and Magnetization Above 300 K in a Bulk Layered Perovskite. *Science* **2015**, *347*, 420−424.
(9) Oh, Y. S.; Luo, X.; Huang, F. T.; Wang, Y.; Cheong, S. W. Experimental Demonstration of Hybrid Improper Ferroelectricity and the Presence of Abundant Charged Walls in $(Ca,Sr)_3Ti_2O_7$ Crystal. *Nat. Mater.* **2015**, *14*, 407−413.
(10) Young, J.; Moon, E. J.; Mukherjee, D.; Stone, G.; Gopalan, V.; Alem, N.; May, S. J.; Rondinelli, J. M. Polar Oxides without Inversion Symmetry through Vacancy and Chemical Order. *J. Am. Chem. Soc.* **2017**, *139*, 2833−2841.
(11) Dion, M.; Ganne, M.; Tournoux, M. New Families of Phases $M^{I}M^{II}_2Nb_3O_{10}$ Consisting of "Perovskite" Sheets. *Mater. Res. Bull.* **1981**, *16*, 1429−1435.
(12) Jacobson, A. J.; Johnson, J. W.; Lewandowski, J. T. Interlayer Chemistry Between Thick Transition-Metal Oxide Layers: Synthesis and Intercalation Reactions of $K[Ca_2Na_{n-3}Nb_nO_{3n+1}]$ $(3 \leq n \leq 7)$. *Inorg. Chem.* **1985**, *24*, 3727−3729.
(13) Kodenkandath, T. A.; Lalena, J. N.; Zhou, W. L.; Carpenter, E. E.; Sangregorio, C.; Falster, A. U.; Simmons, W. B., Jr.; O'Connor, C. J.; Wiley, J. B. Assembly of Metal-Anion Arrays Within a Perovskite Host. Low-Temperature Synthesis of New Layered Copper-Oxyhalides, $(CuX)LaNb_2O_7$, X = Cl, Br. *J. Am. Chem. Soc.* **1999**, *121*, 10743−10746.
(14) Viciu, L.; Caruntu, G.; Royant, N.; Koenig, J.; Zhou, W. L.; Kodenkandath, T. A.; Wiley, J. B. Formation of Metal-Anion Arrays within Layered Perovskite Hosts. Preparation of a Series of New Metastable Transition-metal Oxyhalides, $(MCl)LaNb_2O_7$ (M = Cr, Mn, Fe, Co). *Inorg. Chem.* **2002**, *41*, 3385−3388.
(15) Viciu, L.; Koenig, J.; Spinu, L.; Zhou, W. L.; Wiley, J. B. Insertion of a Two-Dimensional Iron-Chloride Network Between Perovskite Blocks. Synthesis and Characterization of the Layered Oxyhalide, $(FeCl)LaNb_2O_7$. *Chem. Mater.* **2003**, *15*, 1480−1485.
(16) Viciu, L.; Golub, V. O.; Wiley, J. B. Structural, Thermal and Magnetic Characterization of the Manganese Oxyhalide Layered Perovskite, $(MnCl)LaNb_2O_7$. *J. Solid State Chem.* **2003**, *175*, 88−93.
(17) Sanjaya Ranmohotti, K. G.; Montasserasadi, M. D.; Choi, J.; Yao, Y.; Mohanty, D.; Josepha, E. A.; Adireddy, S.; Caruntu, G.; Wiley, J. B. Room Temperature Oxidative Intercalation with Chalcogen Hydrides: Two-Step Method for the Formation of Alkali-Metal Chalcogenide Arrays within Layered Perovskites. *Mater. Res. Bull.* **2012**, *47*, 1289−1294.
(18) Suzuki, H.; Notsu, K.; Takeda, Y.; Sugimoto, W.; Sugahara, Y. Reactions of Alkoxyl Derivatives of a Layered Perovskite with Alcohols: Substitution Reactions on the Interlayer Surface of a Layered Perovskite. *Chem. Mater.* **2003**, *15*, 636−641.
(19) Takeda, Y.; Momma, T.; Osaka, T.; Kuroda, K.; Sugahara, Y. Organic Derivatives of the Layered Perovskite $HLaNb_2O_7{\cdot}xH_2O$ with Polyether Chains on the Interlayer Surface: Characterization, Intercalation of $LiClO_4$, and Ionic Conductivity. *J. Mater. Chem.* **2008**, *18*, 3581−3587.
(20) Takeda, Y.; Suzuki, H.; Notsu, K.; Sugimoto, W.; Sugahara, Y. Preparation of a Novel Organic Derivative of the Layered Perovskite Bearing $HLaNb_2O_7{\cdot}nH_2O$ Interlayer Surface Trifluoroacetate Groups. *Mater. Res. Bull.* **2006**, *41*, 834−841.
(21) Yoshioka, S.; Takeda, Y.; Uchimaru, Y.; Sugahara, Y. Hydrosilylation in the 2D Interlayer Space Between Inorganic Layers: Reaction Between Immobilized C═C Groups on the Interlayer Surface of Layered Perovskite $HLaNb_2O_7{\cdot}xH_2O$ and Chlorohydrosilanes. *J. Organomet. Chem.* **2003**, *686*, 145−150.
(22) Shimada, A.; Yoneyama, Y.; Tahara, S.; Mutin, P. H.; Sugahara, Y. Interlayer Surface Modification of the Protonated Ion-Exchangeable Layered Perovskite $HLaNb_2O_7{\cdot}xH_2O$ with Organophosphonic Acids. *Chem. Mater.* **2009**, *21*, 4155−4162.
(23) Fennie, C. J.; Rabe, K. M. Ferroelectricity in the Dion-Jacobson $CsBiNb_2O_7$ from First Principles. *Appl. Phys. Lett.* **2006**, *88*, 262902.
(24) Benedek, N. A. Origin of Ferroelectricity in a Family of Polar Oxides: The Dion-Jacobson Phases. *Inorg. Chem.* **2014**, *53*, 3769−3777.
(25) Kresse, G.; Hafner, J. Ab initio Molecular Dynamics for Liquid Metals. *Phys. Rev. B: Condens. Matter Mater. Phys.* **1993**, *47*, 558−561.
(26) Kresse, G.; Hafner, J. Ab initio Molecular-Dynamics Simulation of the Liquid-Metal−Amorphous-Semiconductor Transition in Germanium. *Phys. Rev. B: Condens. Matter Mater. Phys.* **1994**, *49*, 14251−14269.
(27) Kresse, G.; Furthmüller, J. Efficiency of ab-initio Total Energy Calcualtions for Metals and Semiconductors Using a Plane-Wave Basis Set. *Comput. Mater. Sci.* **1996**, *6*, 15−50.
(28) Kresse, G.; Furthmüller, J. Efficient Iterative Schemes for ab initio Total-Energy Calculations Using a Plane-Wave Basis Set. *Phys. Rev. B: Condens. Matter Mater. Phys.* **1996**, *54*, 11169−11186.
(29) Perdew, J. P.; Ruzsinszky, A.; Csonka, G. I.; Vydrov, O. A.; Scuseria, G. E.; Constantin, L. A.; Zhou, X.; Burke, K. Restoring the Density-Gradient Expansion for Exchange in Solids and Surfaces. *Phys. Rev. Lett.* **2008**, *100*, 136406.
(30) Blöchl, P. E. Projector Augmented-Wave Method. *Phys. Rev. B: Condens. Matter Mater. Phys.* **1994**, *50*, 17953−17979.
(31) Kresse, G.; Joubert, D. From Ultrasoft Pseudopotentials to the Projector Augmented-Wave Method. *Phys. Rev. B: Condens. Matter Mater. Phys.* **1999**, *59*, 1758−1775.
(32) Resta, R.; Posternak, M.; Baldereschi, A. Towards a Quantum Theory of Polarization in Ferroelectrics: The Case of $KNbO_3$. *Phys. Rev. Lett.* **1993**, *70*, 1010−1013.
(33) Stokes, H. T.; Hatch, D. M.; Campbell, B. J. *ISOTROPY* Software Suite, iso.byu.edu; 2007.
(34) Aroyo, M. I.; Perez-Mato, J. M.; Capillas, C.; Kroumova, E.; Ivantchev, S.; Madariaga, G.; Kirov, A.; Wondratschek, H. Bilbao Crystallographic Server. I Databases and Crystallographic Computing Programs. *Z. Kristallogr. - Cryst. Mater.* **2006**, *221*, 15−27.
(35) Aroyo, M. I.; Kirov, A.; Capillas, C.; Perez-Mato, J. M.; Wondratschek, H. Bilbao Crystallographic Server. II. Representations of Crystallographic Point Groups and Space Groups. *Acta Crystallogr., Sect. A: Found. Crystallogr.* **2006**, *62*, 115−128.
(36) Larson, A. C.; Von Dreele, R. B. *General Structure Analysis System (GSAS)*, Los Alamos National Laboratory Report LAUR 86-748; 2000.
(37) Ok, K. M.; Chi, E. O.; Halasyamani, P. S. Bulk Characterization Methods for Non-Centrosymmetric Materials: Second-Harmonic Generation, Piezoelectricity, Pyroelectricity, and Ferroelectricity. *Chem. Soc. Rev.* **2006**, *35*, 710−717.
(38) Benedek, N. A.; Fennie, C. J. Hybrid Improper Ferroelectricity: A Mechanism for Strong Polarization-Magnetization Coupling. *Phys. Rev. Lett.* **2011**, *106*, 107204.

DOI: 10.1021/acs.chemmater.7b03604
Chem. Mater. 2017, 29, 9489−9497

(39) Benedek, N. A.; Mulder, A. T.; Fennie, C. J. Polar Octahedral Rotations: A Path to New Multifunctional Materials. *J. Solid State Chem.* **2012**, *195*, 11−20.
(40) Mulder, A. T.; Benedek, N. A.; Rondinelli, J. M.; Fennie, C. J. Turning ABO_3 Antiferroelectrics into Ferroelectrics: Design Rules for Practical Rotation-Driven Ferroelectricity in Double Perovskites and $A_3B_2O_7$ Ruddlesden-Popper Compounds. *Adv. Funct. Mater.* **2013**, *23*, 4810−4820.
(41) Snedden, A.; Knight, K. S.; Lightfoot, P. Structural Distortions in the Layered Perovskites $CsANb_2O_7$ (A = Nd, Bi). *J. Solid State Chem.* **2003**, *173*, 309−313.
(42) Goff, R. J.; Keeble, D.; Thomas, P. A.; Ritter, C.; Morrison, F. D.; Lightfoot, P. Leakage and Proton Conductivity in the Predicted Ferroelectric $CsBiNb_2O_7$. *Chem. Mater.* **2009**, *21*, 1296−1302.
(43) Dixon, C. A. L.; McNulty, J. A.; Knight, K. S.; Gibbs, A. S.; Lightfoot, P. Phase Transition Behavior of the Layered Perovskite $CsBi_{0.6}La_{0.4}Nb_2O_7$: A Hybrid Improper Ferroelectric. *Crystals* **2017**, *7*, 135.
(44) Perez-Mato, J. M.; Aroyo, M.; García, A.; Blaha, P.; Schwarz, K.; Schweifer, J.; Parlinski, K. Competing Structural Instabilities in the Ferroelectric Aurivillius Compound $SrBi_2Ta_2O_9$. *Phys. Rev. B: Condens. Matter Mater. Phys.* **2004**, *70*, 214111.
(45) Birenbaum, A. Y.; Ederer, C. Potentially Multiferroic Aurivillius Phase $Bi_5FeTi_3O_{15}$: Cation Site Preference, Electric Polarization, and Magnetic Coupling from First Principles. *Phys. Rev. B: Condens. Matter Mater. Phys.* **2014**, *90*, 214109.
(46) Djani, H.; Bousquet, E.; Kellou, A.; Ghosez, P. First-Principles Study of the Ferroelectric Aurivillius Phase Bi_2WO_6. *Phys. Rev. B: Condens. Matter Mater. Phys.* **2012**, *86*, 054107.
(47) Djani, H.; Hermet, P.; Ghosez, P. First-Principles Characterization of the $P2_1ab$ Ferroelectric Phase of Aurivillius Bi_2WO_6. *J. Phys. Chem. C* **2014**, *118*, 13514−13524.
(48) Etxebarria, I.; Perez-Mato, J. M.; Boullay, P. The Role of Trilinear Couplings in the Phase Transitions of Aurivillius Compounds. *Ferroelectrics* **2010**, *401*, 17−23.
(49) Knapp, M. C.; Woodward, P. M. A-Site Cation Ordering in $AA'BB'O_6$ Perovskites. *J. Solid State Chem.* **2006**, *179*, 1076−1085.
(50) King, G.; Thimmaiah, S.; Dwivedi, A.; Woodward, P. M. Synthesis and Characterization of New $AA'BWO_6$ Perovskites Exhibiting Simultaneous Ordering of A-Site and B-Site Cations. *Chem. Mater.* **2007**, *19*, 6451−6458.
(51) King, G.; Woodward, P. M. Cation Ordering in Perovskites. *J. Mater. Chem.* **2010**, *20*, 5785−5796.
(52) Fukushima, T.; Stroppa, A.; Picozzi, S.; Perez-Mato, J. M. Large Ferroelectric Polarization in the New Double Perovskite $NaLaMnWO_6$ Induced by Non-Polar Instabilities. *Phys. Chem. Chem. Phys.* **2011**, *13*, 12186−12190.
(53) Rondinelli, J. M.; Fennie, C. J. Octahedral Rotation-Induced Ferroelectricity in Cation Ordered Perovskites. *Adv. Mater.* **2012**, *24*, 1961−1968.
(54) Bousquet, E.; Dawber, M.; Stucki, N.; Lichtensteiger, C.; Hermet, P.; Gariglio, S.; Triscone, J.-M.; Ghosez, P. Improper Ferroelectricity in Perovskite Oxide Artificial Superlattices. *Nature* **2008**, *452*, 732−736.
(55) Li, B.; Osada, M.; Ozawa, T. C.; Sasaki, T. $RbBiNb_2O_7$: A New Lead-Free High-T_C Ferroelectric. *Chem. Mater.* **2012**, *24*, 3111−3113.
(56) Chen, C.; Ning, H.; Lepadatu, S.; Cain, M.; Yan, H.; Reece, M. J. Ferroelectricity in Dion-Jacobson $ABiNb_2O_7$ (A = Rb, Cs) Compounds. *J. Mater. Chem. C* **2015**, *3*, 19−22.
(57) Strayer, M. E.; Sen Gupta, A.; Akamatsu, H.; Lei, S.; Benedek, N. A.; Gopalan, V.; Mallouk, T. E. Emergent Noncentrosymmetry and Piezoelectricity Driven by Oxygen Octahedral Rotations in n = 2 Dion-Jacobson Phase Layer Perovskites. *Adv. Funct. Mater.* **2016**, *26*, 1930−1937.
(58) Sim, H.; Kim, B. G. Octahedral Tilting and Ferroelectricity in $RbANb_2O_7$ (A = Bi, Nd) From First Principles. *Phys. Rev. B: Condens. Matter Mater. Phys.* **2014**, *89*, 144114.
(59) Machida, M.; Yabunaka, J. I.; Kijima, T. Efficient Photocatalytic Decomposition of Water with the Novel Layered Tantalate $RbNdTa_2O_7$. *Chem. Commun.* **1999**, 1939−1940.
(60) Machida, M.; Yabunaka, J. I.; Kijima, T. Synthesis and Photocatalytic Property of Layered Perovskite Tantalates, $RbLnTa_2O_7$ (Ln = La, Pr, Nd, and Sm). *Chem. Mater.* **2000**, *12*, 812−817.
(61) Machida, M.; Miyazaki, K.; Matsushima, S.; Arai, M. Photocatalytic Properties of Layered Perovskite Tantalates, $MLnTa_2O_7$ (M = Cs, Rb, Na and H; Ln = La, Pr, Nd, and Sm). *J. Mater. Chem.* **2003**, *13*, 1433−1437.
(62) Dion, M.; Ganne, M.; Tournoux, M. The Layered Ferroelastic Perovskite $M^I(A_{n-1}Nb_nO_{3n+1})$ Terms *n* = 2, 3 and 4. *Rev. Chim. Miner.* **1986**, 61−69.
(63) Kodenkandath, T. A.; Kumbhar, A. S.; Zhou, W. L.; Wiley, J. B. Construction of Copper Halide Networks within Layered Perovskites. Syntheses and Characterization of New Low-Temperature Copper Oxyhalides. *Inorg. Chem.* **2001**, *40*, 710−714.
(64) Glazer, A. M. The Classification of Tilted Octahedra in Perovskites. *Acta Crystallogr., Sect. B: Struct. Crystallogr. Cryst. Chem.* **1972**, *28*, 3384−3392.
(65) Stokes, H. T.; Hatch, D. M.; Wells, J. D. Group-Theoretical Methods for Obtaining Distortions in Crystals: Applications to Vibrational Modes and Phase Transitions. *Phys. Rev. B: Condens. Matter Mater. Phys.* **1991**, *43*, 11010.
(66) Hatch, D. M.; Stokes, H. T. Complete Listing of Order Parameters for a Crystalline Phase Transition: A Solution to the Generalized Inverse Landau Problem. *Phys. Rev. B: Condens. Matter Mater. Phys.* **2001**, *65*, 014113.
(67) Howard, C. J.; Stokes, H. T. Structures and Phase Transitions in Perovskites − A Group-Theoretical Approach. *Acta Crystallogr., Sect. A: Found. Crystallogr.* **2005**, *61*, 93−111.
(68) Stengel, M.; Fennie, C. J.; Ghosez, P. Electrical Properties of Improper Ferroelectrics from First Principles. *Phys. Rev. B: Condens. Matter Mater. Phys.* **2012**, *86*, 094112.
(69) Benedek, N. A.; Rondinelli, J. M.; Djani, H.; Ghosez, P.; Lightfoot, P. Understanding Ferroelectricity in Layered Perovskites: New Ideas and Insights from Theory and Experiments. *Dalton Trans.* **2015**, *44*, 10543−10558.
(70) Young, J.; Stroppa, A.; Picozzi, S.; Rondinelli, J. M. Anharmonic Lattice Interactions in Improper Ferroelectrics for Multiferroic Design. *J. Phys.: Condens. Matter* **2015**, *27*, 283202.
(71) Cohen, R. E. Origin of Ferroelectricity in Perovskite Oxides. *Nature* **1992**, *358*, 136−138.
(72) Armstrong, A. R.; Anderson, P. A. Synthesis and Structure of a New Layered Niobium Blue Bronze: $Rb_2LaNb_2O_7$. *Inorg. Chem.* **1994**, *33*, 4366−4369.

DOI: 10.1021/acs.chemmater.7b03604
Chem. Mater. 2017, 29, 9489−9497